Characterization of the Electron- and Photon-Driven Plasmonic Excitations of Metal Nanorods

Nicholas W. Bigelow,[†] Alex Vaschillo,[†] Vighter Iberi,[‡] Jon P. Camden,[‡,*] and David J. Masiello[†,*]

[†]Department of Chemistry, University of Washington, Seattle, Washington 98195-1700, United States and [‡]Department of Chemistry, University of Tennessee, Knoxville, Tennessee 37996-1600, United States

The mechanisms by which a swift ion can deposit energy into metallic films, spawning both individual and collective electronic excitations, have been well established.[1−5] The experimental techniques developed to probe these phenomena and their related theoretical underpinnings are now seeing a renaissance in the fields of nanophotonics and nanoplasmonics. Recent experimental interrogation of nanoscopic metal triangular prisms,[6−8] spheres,[9,10] rods,[11−13] cubes,[14] and decahedra[15] with swift electrons has exposed a variety of new information that is not resolvable with standard optical techniques alone. The observation of optically dark plasmonic modes[10,13] evidences the differing selection rules between electron- and photon-excitation sources. Also, the direct spatial mapping of plasmon resonances and, with correlated optical techniques, their associated evanescent near-field and electromagnetic far-field demonstrates the unique resolving power of the electron.[16,17] Still, questions remain that call for the implementation of theories capable of describing the electron-driven excitation of plasmonic nanoparticle assemblies of arbitrary geometry, aggregation scheme, and material composition. Examples include the following: (1) Is there a difference between the plasmons generated at the same excitation energy but by an electron rather than a photon source? (2) What is the difference between their associated evanescent near-fields? (3) How similar are their far-fields? (4) What is the signature of electromagnetic hot spots in EELS and what is their relationship to optical excitation?

In the following, we address these questions within the context of monomer and dimer silver nanorods using an electron-scattering theory based upon a modification[5] of the discrete-dipole approximation (DDA).[18,19] An interesting result of our work is that EELS

ABSTRACT
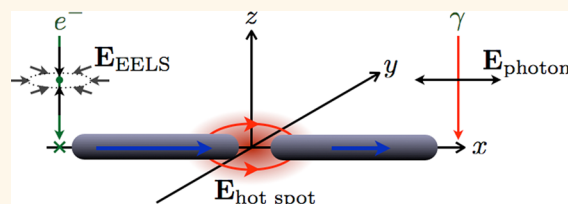
A computational analysis of the electron- and photon-driven surface-plasmon resonances of monomer and dimer metal nanorods is presented to elucidate the differences and similarities between the two excitation mechanisms in a system with well-understood optical properties. By correlating the nanostructure's simulated electron energy-loss spectrum and loss-probability maps with its induced polarization and scattered electric field we discern how certain plasmon modes are selectively excited and how they funnel energy from the excitation source into the near- and far-field. Using a fully retarded electron-scattering theory capable of describing arbitrary three-dimensional nanoparticle geometries, aggregation schemes, and material compositions, we find that electron energy-loss spectroscopy (EELS) is able to *indirectly* probe the same electromagnetic hot spots that are generated by an optical excitation source. Comparison with recent experiment is made to verify our findings.

KEYWORDS: electron energy-loss spectroscopy · localized surface plasmon · silver nanoparticles · scanning transmission electron microscopy · hot spots

is capable of *indirectly* probing electromagnetic hot spots, such as those responsible for surface-enhanced Raman scattering (SERS). Our argument, which relies upon correlating electron and photon spectroscopies, is that the spatial locations of high electron energy-loss and intense photonic near-fields need not be colocated; yet they are related in a simple way by noticing that the near-field generated by an electron probe, when positioned properly, is directionally identical to that set up by an optical source. Recent experiment is consistent with this prediction.[20]

The motion of a swift ion generates an electric field whose structure and dynamics are governed by the equation of

© 2012 American Chemical Society

motion[21]

$$\nabla \times \nabla \times \mathbf{E} + \varepsilon\mu\ddot{\mathbf{E}}/c^2 = -4\pi\mu\dot{\mathbf{J}}/c \qquad (1)$$

Accordingly, an electron of charge $-e$ moving uniformly along the trajectory $\mathbf{r}(t) = \mathbf{v}t$ imposes the field

$$\mathbf{E}_{EELS}(\mathbf{x},\omega) = \frac{2e\omega}{v^2\varepsilon\gamma}e^{i\omega z/v}\left[\frac{i}{\gamma}K_0\left(\frac{\omega b}{v\gamma}\right)\hat{\mathbf{v}} - K_1\left(\frac{\omega b}{v\gamma}\right)\hat{\mathbf{b}}\right]$$
(2)

upon a point $\mathbf{x}$ located a distance $|\mathbf{x}| = (|\mathbf{b}|^2 + z^2)^{1/2}$ away from its path. The structure of this field is markedly different from that of a plane wave in that it has polarization components perpendicular to ($\hat{\mathbf{b}} \perp \hat{\mathbf{v}}$) and along the direction of propagation ($\hat{\mathbf{v}} \parallel \hat{\mathbf{e}}_z$). Both components decay radially as the modified Bessel functions K_0 and K_1, and are not spatially isotropic for $v < c$. Rather the electric field of the electron is spatially localized and spectrally broadband, exactly the opposite of the spatially isotropic and monochromatic plane wave. Experiments like EELS exploit these unique electromagnetic properties by using electrons with keV kinetic energies to probe the electronic structure of matter with sub-angstrom spatial resolution.[22] Such experiments[6−17] and their correlation with optical spectroscopies now represent the next generation of light-matter interaction in nanoplasmonics and nanophotonics offering unprecedented spatial, spectral, and temporal resolution.

Metal nanorods with high aspect ratios and their aggregates serve as a good test bed for our numerical approach as they support a clear progression of longitudinal multipolar plasmon resonances that hybridize in a straightforward manner upon aggregation.[23] The symmetry of the rod establishes electronic density disturbances that are eigenfunctions of parity, that is, $\Pi\Omega_{g,u}(\mathbf{x}) = \Omega_{g,u}(-\mathbf{x}) = \pm\Omega_{g,u}(\mathbf{x})$. One would expect that only the transitions $\langle\Omega_u|\mathbf{x}|\Psi_0\rangle$ from the many-electron (symmetric) ground state Ψ_0 of the metal to transient, odd-parity plasmons Ω_u will be dipole-allowed, whereas those transitions to even-parity plasmons Ω_g, which have no net dipole moment, will be forbidden. This is the case for a plane-wave excitation source in the so-called long-wavelength or electric-dipole interaction approximation. However, this approximation is inappropriate for electron-driven transitions because the variation of the electron's associated electric field over the target is significant and, further, carries a wavelength that is reduced by a factor of v/c in comparison to a photon of the same energy. Because of this, the electron source is able to probe transitions that are optically inaccessible.[10,13]

Our numerical approach, which we call electron-driven DDA (e-DDA), imposes the exciting electric field $\mathbf{E}_{EELS}$ of a swift electron eq 2 instead of a plane wave upon each point $\mathbf{x}_j$ of the target.[5] Through electric-dipole radiation each dipole couples to all others in the

same manner as in the DDA, yielding a similar

$$\sum_{k=1}^{N}[\boldsymbol{\alpha}_{jk}^{-1}(\omega) - (1 - \delta_{jk})\boldsymbol{\Lambda}_{jk}]\cdot\mathbf{P}_k(\omega) = \mathbf{E}_{EELS}(\mathbf{x}_j, \omega) \quad (3)$$

problem for every spatial position $\mathbf{b}$ of the electron beam with respect to the target, the latter described by its bulk dielectric function $\varepsilon(\omega)$ through the linear polarizability $\boldsymbol{\alpha}_{jk}(\omega) \equiv \boldsymbol{\alpha}_j(\varepsilon(\omega))\delta_{jk}$ of each point j. Iterative solution of these e-DDA equations from the initial guess $\mathbf{P}_j = \mathbf{0}_j$ at each ω determines the polarization induced in the target by the loss of energy $\hbar\omega$ from the electron beam.

The probability per unit energy $P_\mathbf{b}$ for the incident electron to lose kinetic energy is determined from the rate of doing work by the electric field of the electron back upon itself, that is, $dW/dt = \int_V \mathbf{J}\cdot\mathbf{E}_{EELS}\,d^3x$. Assuming that the electron undergoes no recoil as it moves along its trajectory, its current density becomes $\mathbf{J}(\mathbf{x},t) = -e\mathbf{v}\delta(\mathbf{x} - \mathbf{v}t)$, which leads to the following loss probability,[5]

$$P_\mathbf{b}(\hbar\omega) = \frac{1}{\pi\hbar^2}\,\mathrm{Im}\sum_{j,k=1}^{N}\mathbf{E}_{EELS}^*(\mathbf{x}_j, \omega)$$
$$\cdot[\boldsymbol{\alpha}^{-1}(\omega) - (1 - \delta)\boldsymbol{\Lambda}]_{jk}^{-1}\cdot\mathbf{E}_{EELS}(\mathbf{x}_k, \omega) \qquad (4)$$

Computation of $P_\mathbf{b}$ allows us to determine the energy-loss spectrum of each spatial point $\mathbf{b}$ in the plane of the target in direct analogy to experiments where the scanning transmission electron microscope (STEM) is rastered over the target and the energy-loss spectrum of the electron is collected at each point. We emphasize that this e-DDA allows us to compute the fully retarded electron-driven plasmonic responses of a three-dimensional nanoparticle assembly of arbitrary geometry, aggregation scheme, and material composition. This differs from other recent theoretical approaches to EELS that work within the quasi-static approximation to study idealized, flat, disk-shaped nanoparticles,[24] or that antisymmetrize the polarization of the plane wave to mimic the transverse polarization of the electron's electric field.[10] The e-DDA is, however, similar to the coupled-dipole/DDA approach implemented by Geuquet and Henrard,[25] with the main difference being that we work within the existing framework of Draine's DDSCAT code[19] to numerically implement the working equations in parallel. The flexibility and efficiency of the existing algorithm, which relies upon a biconjugate gradient method for the iterative solution of eq 3, allow us to easily extract the plasmonic polarization and scattered electromagnetic field at any point in space induced by the loss of energy from a passing swift electron. This e-DDA approach should compare similarly to other rigorous and efficient theoretical/numerical approaches to EELS such as the boundary-element[26] and T-matrix[27] methods. Both map the full three-dimensional electromagnetic scattering problem onto a two-dimensional

boundary-value problem defined at the interface between dielectric media. Also, an implementation of EELS in COMSOL has recently been reported;[28] however, due to the brevity of its description it is difficult to compare to the e-DDA.

RESULTS AND DISCUSSION

EELS Spectra and Maps. Figure 1 presents the e-DDA-based EELS spectrum (black) of a 202 nm × 40 nm silver nanorod supported upon an amorphous SiN_x substrate. The propagation direction of the 0.1 MeV electron beam is oriented normal to long axis of the
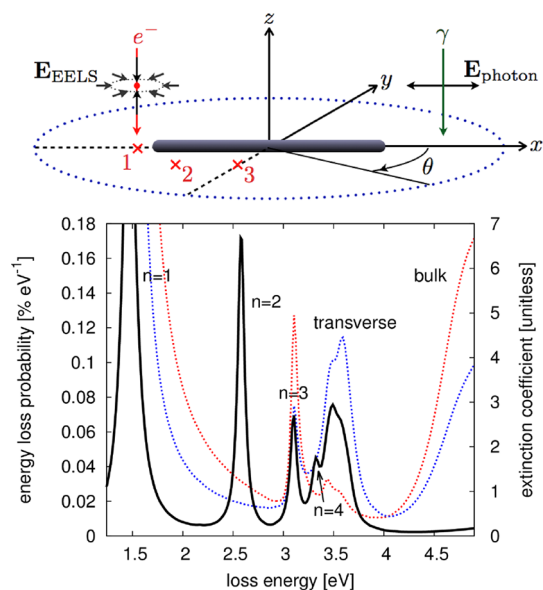

Figure 1. Energy loss spectrum (black) of a 202 nm × 40 nm silver nanorod on an amorphous SiN_x substrate. The rod is excited by a 0.1 MeV electron beam positioned 1 nm away from the rod's tip as indicated by position 1 in the upper panel. The beam is propagating normal to the plane of the substrate (not shown). For comparison, the optical extinction spectrum of the rod is displayed in the background. The red (blue) curve corresponds to light propagating normal to the substrate and polarized along ($\theta = 45°$ with respect to) the rod axis. The four lowest energy resonances correspond to the lowest-lying longitudinal plasmon modes of which the first ($n = 1$) and third ($n = 3$) are optically bright and the second ($n = 2$) and fourth ($n = 4$) are optically dark. The latter two are absent in the optical extinction spectrum.
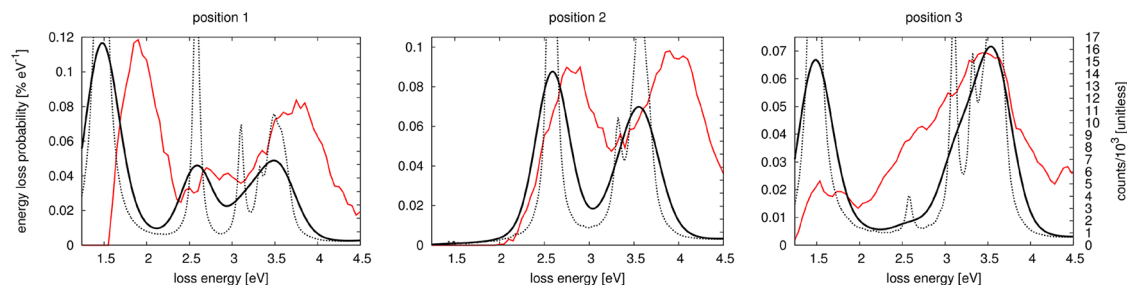
rod (also normal to the substrate, which is not shown) as shown in the upper panel of the figure. For comparison, the computed optical extinction spectra for light propagating normal to the substrate and polarized both along (red) and $\theta = 45°$ (blue) from the rod axis are also displayed across the same spectral range using the DDA. A progression of collective electronic resonances arise in the low loss-energy part of the spectrum corresponding to the excitation of multipolar surface plasmons that are spatially delocalized along the longitudinal axis of the rod. Interestingly, while the EELS spectrum shows both odd and even order plasmonic resonances, the optical resonance features skip all even orders because their wave functions exhibit no net dipole moment and are, therefore, optically dark. Indeed, the consequences of plasmon symmetry are immediately evident in comparing the electronic and optical spectra of the nanorod. At higher loss-energies near 3.5 eV, surface-plasmon resonances that oscillate transverse to the rod's long axis are excited by the $\hat{\mathbf{v}}$-dependence of the polarization eq 2, before the excitation of the bulk plasmon at even higher energies.

A set of silver nanorods similar to this was recently characterized under STEM/EELS by Guiton, Camden, and co-workers.[11] Their experiment correlated, for the first time, EELS plasmon maps with optical scattering from the exact same nanoparticles. Figure 2 displays the experimental EELS spectra (red) measured at three different spatial points surrounding the rod as shown in the upper panel of Figure 1. EEL spectra computed at the same three points are displayed in the background as the dotted black curves. For comparison between the two spectra, each point is convolved with a Gaussian function having a full width at half-maximum of 0.4 eV (blue), the area of which is equal to the computed loss probability at that point. The width of 0.4 eV is not an adjustable parameter, but rather is dictated by the resolution of the STEM/EELS instrument. No shifting is performed on either the computed or observed spectra, yet their agreement is quite good. Some reasons for the differences between the spectra, particularly at low loss-energies, may be due to the fact that the zero-loss peak must be subtracted from the
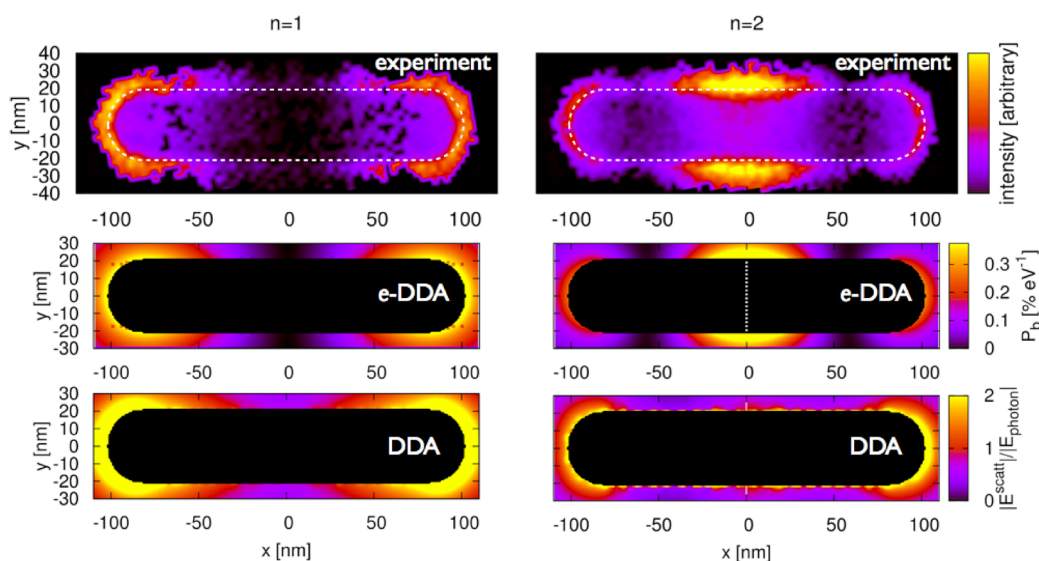

Figure 2. Experimental (red, right vertical axis) and theoretical (black, left vertical axis) EEL spectra corresponding to three positions of the electron beam as shown in the upper panel of Figure 1. To mimic the instrumental resolution, each point in the computed spectra (dotted black) is convoluted with a Gaussian function whose full width at half-maximum is 0.4 eV (solid black). The height of each Gaussian at each spectral point is chosen so that its area is equal to the corresponding loss probability at that point.

Figure 3. Loss-probability maps of the two lowest-lying longitudinal plasmon modes of a silver nanorod supported on an amorphous SiN_x substrate. $n = 1$ (1.50 eV) and $n = 2$ (2.61 eV) correspond to the first bright and dark plasmon modes of the monomer. The upper two panels display the experimentally measured loss-probability maps, adapted from ref 11, while the middle two panels display the same observable computed *via* the *e*-DDA. Each map indicates where in space the incident electron is likely to deposit the fraction $\hbar\omega$ of its initial 0.1 MeV kinetic energy into a multipolar plasmon mode. The white dotted line in the middle right panel indicates the spatial location of the node of the first dark plasmon mode of the rod monomer. The lower two panels display the magnitudes of the corresponding electric fields scattered from the rod after excitation by a plane wave, computed *via* the DDA; these near-field magnitudes are taken in ratio to the magnitude of the incident plane wave, E_{photon}. For the $n = 1$ mode, the incident field's direction of propagation (electric polarization) is normal (parallel) to the long axis of the rod. While for the $n = 2$ mode, the incident field propagation and polarization directions lie in the plane of the long axis of the rod and its normal, but are tilted by $\pm 45°$ with respect to the normal. This arrangement allows for light to couple into a mode of the rod that is dark under normal incidence. To symmetrize the $n = 2$ scattered electric field, we average together both $\pm 45°$-polarizations.[11] It is clear that the loss-probability maps (upper four panels) and the photonic local density of states,[29] which is related to the scattered electric field magnitude[30] (bottom two panels), are not simply related to each other in this case.[24,31]

experimental EEL spectrum. In general, this is a difficult task even with good signal-to-noise ratios. Small imperfections in the shape of the rod and/or substrate can alter the rod's local dielectric function, thereby affecting the EELS spectrum. This, in addition to the distance/angle between rod and substrate, is challenging to quantify experimentally and, therefore, was not accounted for in the computations. Also, it is not unreasonable to speculate that the electron beam is damaging the target and/or the substrate, providing a further spatial-dependent modification of the dielectric functions of each.[10]

At the energy of the two lowest-lying longitudinal plasmon resonances of the rod monomer (Figure 1) and dimer (not shown) we compute a spatial mapping of the loss probability P_b. The dimer is oriented along the x axis and is composed of colinear 111 nm × 11 nm monomer subunits separated by a 1 nm gap. For both monomer and dimer, P_b is projected onto the plane that bisects the long axis of the rod and that is perpendicular to the direction of propagation of the electron beam. This requires solving eq 4 across a two-dimensional grid of impact parameters **b** surrounding the target. Its pattern shows where in space the electron is likely to deposit the fraction $\hbar\omega$ of its initial 0.1 MeV kinetic energy. By computing the electronic polarization induced in the target by the electron beam

we see that the regions of high loss-probability occur at the characteristic nodes of each plasmonic wave function and at the rod ends, which are also effectively nodes. This is because the longitudinal components of the electric force $F_\parallel = -eE_\parallel$ exerted by the electron beam maximally coincide with the opposing plasmonic polarization vectors at each node of the plasmon wave function. This means that the potential energy of interaction between the polarization of the electron beam's electric field and the polarization of the plasmonic target is minimized at the position of each node. Depending upon the magnitude of the loss-energy, $\hbar\omega$, different multipolar plasmons are excited, each with its own nodal structure (*i.e.*, no nodes, 1 node, 2 nodes, *etc.*) and associated loss probability map.

In Figure 3, we compare the experimentally determined loss-probability maps of the two lowest-lying longitudinal plasmon resonances, labeled $n = 1,2$, of the rod monomer (upper panels) with those computed *via* the *e*-DDA (middle panels). Excellent agreement between these data (as well as for the spectra in Figure 1) indicates that the *e*-DDA provides a reasonable description of these electron-driven plasmonic excitations. For comparison, the lower two panels of Figure 3 display the magnitude of the corresponding electric fields scattered from the rod when driven by a plane wave, computed *via* the DDA. To optically excite

the $n = 2$ plasmon mode, which is dark, we rotate the propagation direction by $\pm 45°$ from the normal in the plane containing the rod's long axis, and average the two scattered fields together to symmetrize the electric field magnitude; this rotation and averaging technique was used previously[11] to explain the observed loss-probability maps of dark plasmon modes. However, here we see that the scattered electric field magnitude misses certain details in the loss-probability map. For example, in the case of the $n = 2$ dark mode, P_b is largest in the middle of the rod and is smaller at the rod's ends; the electric field inverts these trends, even in the case of a monomer.

Figure 4 displays the loss-probability maps of the lowest energy bonding and antibonding plasmon resonances of the rod dimer, computed *via* the e-DDA.
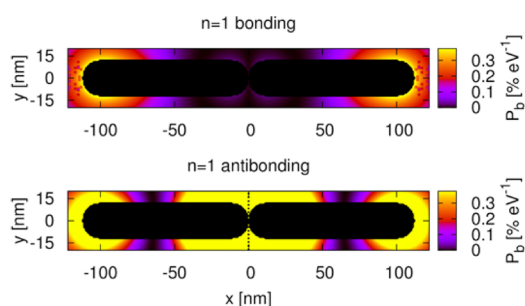

Figure 4. Loss-probability maps of the two lowest-lying longitudinal ($n = 1$ bonding and antibonding) plasmon modes of a silver nanorod dimer supported on an amorphous SiN_x substrate. The rods are arranged to have a 1 nm gap in the junction between monomers. Each map indicates where in space the incident electron is likely to deposit the fraction $\hbar\omega$ of its initial 0.1 MeV kinetic energy into a multipolar plasmon mode. The black dotted line in the lower panel indicates the spatial location of the node of the first antibonding plasmon mode of the rod dimer. For the bonding mode, the loss-probability in the junction is nearly zero, which has led to the belief that EELS is blind to electromagnetic hot spots.[24]

It is important to point out that P_b is nearly zero in the junction of the dimer at the loss-energy corresponding to the bonding mode. Yet when excited by a plane wave at this energy, polarized along the dimer axis, the dimer supports an electromagnetic hot spot in the junction (not shown), implying a corresponding increase in the photonic local density of states. A related observation in the case of flat, disk-shaped dimers, showing the disconnect between EELS and the photonic local density of states, was demonstrated by Hohenester et al.[24] in contrast to earlier work.[31] This has led to the belief that EELS is unable to probe electromagnetic hot spots such as those responsible for SERS.

Electron-Induced Target Polarization and Electric near-Field. It is instructive to visualize the polarization induced in the nanorod target at different loss-energies when the electron beam is fixed at a single point in space. The polarizations (red vectors) of the two lowest-lying longitudinal plasmon resonances of the rod monomer and dimer are displayed in Figure 5 in the plane that bisects the long axis of the rod, and that is perpendicular to the direction of propagation of the electron beam. Interestingly, it is clear that a single position of the electron beam (denoted by an "x") is sufficient to excite a spatially delocalized, multipolar, plasmonic resonance of the rod. Each plasmon mode, being a transient and oscillatory electronic density disturbance, generates a corresponding electromagnetic field as a decay channel by which to remove (conserve) energy. The near-zone scattered electric component of each is displayed in Figure 5 with its magnitude shown in the background and its vector structure indicated by the overlaid white vectors. Because of the localized nature of the excitation source the induced polarizations and scattered electric fields are not symmetric, unlike the corresponding (g,u)
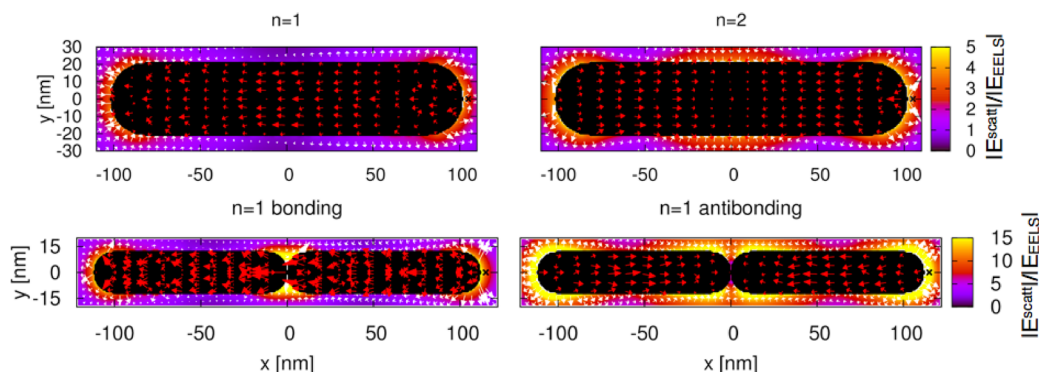

Figure 5. Induced polarization and electric field scattered from the nanorod monomer and dimer upon excitation by a 0.1 MeV electron beam located 1 nm away from the rod's right tip, as indicated by the "x". Both the polarization vectors (red arrows) and electric field vectors (white) and magnitude (background) are plotted in the plane bisecting the rod. Here the near-field magnitude is taken in ratio to the spatially anisotropic exciting field magnitude, corresponding to E_{EELS}. Each map is computed at the loss-energies corresponding to the $n = 1$ (1.50 eV) and $n = 2$ (2.61 eV) bright and dark modes of the monomer and the $n = 1$ bonding (1.50 eV) and antibonding (1.95 eV) modes of the dimer; the former resonances are displayed in Figure 1. Even with electron excitation, an electromagnetic hot spot is formed in the junction of the dimer at the loss-energy corresponding to the $n = 1$ bonding mode.
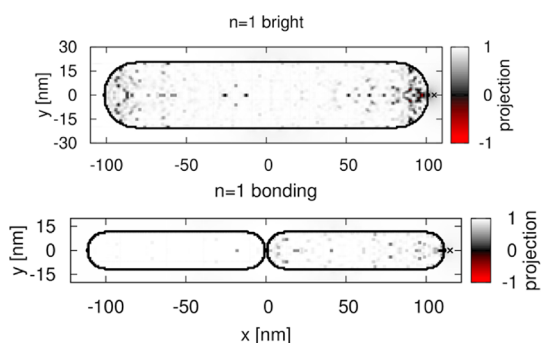
Figure 6. Projections of the electron- and photon-induced polarizations, Δ_P, and the electron- and photon-induced scattered electric near-fields, Δ_E, of the nanorod monomer and dimer. P and E^{scatt} are normalized to have unit length, making the projections a measure of the overlap of their directions only. Both the $n = 1$ monomer and $n = 1$ bonding dimer modes are optically bright. Spatial regions where the two polarization and scattered electric fields are the same (white) or opposite (red) in direction are clearly visible. Interestingly, the $n = 1$ bonding dimer mode shows that the electric field set up in the junction by a swift electron has the same directional dependence as the junction field induced by a plane wave. The position of the electron beam is denoted by an "x" and the polarization of the plane wave is directed along the long axis of the rod.

plasmon eigenmodes induced by a plane wave of the same frequency.

Comparison of the Electron- and Photon-Induced Plasmon Polarizations and Scattered Electric Fields. To compare the nature of the multipolar plasmonic excitations generated by either a photon (plane-wave) or electron (EELS) source at the same excitation energy we define the following overlap measure

$$\Delta_{\mathbf{g}} = \frac{\mathbf{g}_{photon}}{|\mathbf{g}_{photon}|} \cdot \frac{\mathbf{g}_{EELS}}{|\mathbf{g}_{EELS}|} \qquad (5)$$

with $\mathbf{g} = \mathbf{P}$ or $\mathbf{E}^{scatt}$. We choose to normalize the plasmon polarization **P** and scattered electric field $\mathbf{E}^{scatt}$ from both sources to expose the directional dependence of the overlap, independent of their differing magnitudes. Clearly $-1 \leq \Delta_{\mathbf{g}} \leq 1$, with 1 implying that the directionality of $\mathbf{g}_{photon}$ and $\mathbf{g}_{EELS}$ is the same, -1 implying their directionality is opposite, and 0 implying they are orthogonal. Figure 6 displays the projections Δ_P and Δ_E for both the rod monomer and dimer in the plane that bisects the long axis of the rod and that is perpendicular to the direction of propagation of the electron and photon beams. The lowest energy $n = 1$ bright (1.50 eV) and bonding (1.50 eV) plasmonic excitations are chosen for comparison. For both monomer and dimer, the position of the electron beam is indicated by an "x" in the figures, and the polarization of the plane wave is directed along the longitudinal axis of the rod.

It is evident from Δ_P and Δ_E that the optically bright plasmon modes of the monomer and dimer and their associated electric near-fields are almost directionally identical for both excitation sources. In the case of

the dimer, it is important to point out that the electric field in the junction that is set up by the electron-driven bonding plasmon has near unit overlap with the junction field set up by a plane wave at the same energy. This is interesting because it shows that a swift electron can *indirectly* excite a junction field that is similar to the electromagnetic hot spot generated by plane-wave excitation. In fact the two fields are directionally identical. This observation adds a *softening* of the statement that EELS is "completely blind to the hot spot"[24] that was based upon a comparison between EELS and the photonic local density of states. Through our numerical experimentation, comparing EELS to the vector-valued electric field itself, we see that EELS is not blind to hot spots if the observer knows how to correlate the loss probability map to the scattered electric near-field. For example, the loss probability map of the bonding dimer mode is bright at the ends of the dimer (Figure 3), indicating that this is the most efficient way to set up the bonding arrangement of the plasmon polarization needed to generate a capacitive- or hot-spot-like field in the junction. This implies that the location where EELS probes may be spatially separated from where a hot spot is generated. Recent collaborative work with experiment has shown this reasoning to be true even for complex three-dimensional aggregates that are determined to be single-molecule SERS active.[20]

Lastly, we compute the projections, Δ_E, of the scattered electric far-fields induced by electron and photon sources (cathodoluminescence *versus* photoluminescence) for the two lowest energy plasmonic modes of the rod monomer and dimer. For these projections we evaluate $\mathbf{E}^{scatt}$ along a distant circle of radius 2 μm surrounding the target in the plane perpendicular to the direction of propagation of the electron and photon beams; the upper panel of Figure 1 shows a representation of this distant circle in blue. For both the monomer's and dimer's $n = 1$ bright and bonding modes, $\Delta_E \approx 1$ for all angles (not shown). This indicates that the electric field scattered by the monomer and dimer into the far-field are nearly identical in direction for both excitation sources for these modes. Knowing how these near- and far-fields behave suggests an electron-driven version of SERS experiment, where the flow of energy may be tracked between the electron source and a Raman-active molecule located within an electromagnetic hot spot.

CONCLUSION

In summary, we numerically implement the *e*-DDA, adding the exciting electric field of a swift electron[21] to the standard DDA of Draine.[19] This allows us to efficiently compute the plasmon polarization within and the electric field scattered from an arbitrary nano-target excited by an electron source and to correlate these quantities with their photon-induced analogues,

computed *via* the DDA. In our numerical investigations of the nanorod monomer and dimer we learn how both bright and dark multipolar plasmons are selectively excited and how they funnel energy from the near-field to the far-field. We also learn, in the case of the nanorod dimer, that EELS can indirectly indicate the presence and even location of a junction field that is directionally identical to the hot spot set up by plane-wave excitation. This is demonstrated by comparing the loss-probability map to the vector-valued electric near-field, rather than to the photonic local density of states. Recent experiment has demonstrated that this numerical observation on rod dimers is also true for more complex nanostructures.[20]

METHODS

Continuum Electrodynamics Simulations. The DDA is routinely used to study the response of metal nanoparticles subjected to optical-frequency radiation.[32] In this approximation the target is discretized into a finite collection of polarizable point dipoles $\mathbf{P}_j$, $1 \leq j \leq N$, each driven by an exciting plane-polarized electric field as well as by the fully retarded electric-dipole field $\sum_{k \neq j}^{N} \mathbf{\Lambda}_{jk} \cdot \mathbf{P}_k$ generated by all other points; here $\mathbf{\Lambda}_{jk} = e^{ikr_{jk}}\{(1/r_{jk}^3 - ik/r_{jk}^2)[3\hat{\mathbf{n}}_{jk}\hat{\mathbf{n}}_{jk} - \mathbf{1}_{jk}] - k^2\hat{\mathbf{n}}_{jk} \times (\hat{\mathbf{n}}_{jk} \times)/r_{jk}\}$ is the standard dipole tensor that relays the electric field generated by a dipole at one point in space $\mathbf{x}_j$ to another $\mathbf{x}_k$ a distance $r_{jk}\hat{\mathbf{n}}_{jk} = |\mathbf{x}_j - \mathbf{x}_k|\hat{\mathbf{n}}_{jk}$ away. In this manner, the responses of the system that are optically accessible can be computed once each dipole is brought into self-consistency with all others at a certain excitation frequency, ω. This is accomplished through the iterative solution of the following equation,

$$\sum_{k=1}^{N} [\boldsymbol{\alpha}_{jk}^{-1}(\omega) - (1 - \delta_{jk})\mathbf{\Lambda}_{jk}] \cdot \mathbf{P}_k(\omega) = \mathbf{E}_{\text{photon}}(\mathbf{x}_j, \omega) \quad (6)$$

and depends upon the frequency-dependent linear polarizability $\boldsymbol{\alpha}_{jk}(\omega) \equiv \boldsymbol{\alpha}_j(\varepsilon(\omega))\delta_{jk}$ of the target point j. The polarizability is related to the dielectric function through the lattice dispersion relation.[33]

Our numerical approach, which we call *e*-DDA, replaces the exciting field of the plane wave, $\mathbf{E}_{\text{photon}}$, with the that of a swift electron, $\mathbf{E}_{\text{EELS}}$, given in eq 2;[21] $\gamma = 1/(1 - \varepsilon(v/c)^2)^{1/2}$ is the Lorentz factor involving the dielectric function ε of the background medium, which is taken to be vacuum in all calculations, and v is the electron's incident velocity corresponding to the incident kinetic energy $m\gamma c^2 - mc^2$. We choose the phase $e^{i\omega z/v} = 1$ at the z-height of the mass centroid of the target. Otherwise, we use the existing DDSCAT numerical algorithm to solve the resulting *e*-DDA equations. This allows us to efficiently compute the EEL spectra at hundreds to thousands of points surrounding the nanotarget, in parallel. (The *e*-DDA source code is distributed free of charge under the GNU General Public License at http://faculty.washington.edu/masiello).[37]

All *e*-DDA and DDA simulations performed in this article involve nanorods that are supported upon a 5 nm thick amorphous SiN_x substrate. The substrate is located directly below the target, with no gap in between the two media. All target structures are excited by a 0.1 MeV electron beam directed normal to the substrate; the corresponding velocity of the electrons in the beam is 0.55 c. Only points external to the target are considered in the simulations and the two-dimensional grid of impact parameters $\mathbf{b}$ for the electron beam is chosen to have a 1 nm spacing. Dielectric data from Johnson and Christy[34] is used for silver, while those for the substrate are taken from Palik.[35] An interdipole spacing of 1 nm for both target and substrate is used throughout; other dipole spacings were tested to ensure that all spectra are converged at this value. Similarly, all electric fields are evaluated on a grid with 1 nm grid spacing.

STEM/EELS Experiment. A description of the correlated optical and STEM/EELS data collection methods are described in detail elsewhere.[11] Briefly, a 2 μL aliquot of the colloidal nanoparticles is drop-coated onto a TEM grid and allowed to dry in air. The sample is subsequently loaded onto an inverted optical microscope equipped with a dark-field condenser and wide-field imaging camera. Under dark-field conditions, the resonance Rayleigh spectra of the individual nanoparticles are recorded, as well as the wide field images showing the individual particles as diffraction-limited spots. After transferring the sample to an aberration-corrected STEM equipped with EELS, the wide-field images obtained on the optical and electron microscopes are compared and pattern-matching is used to determine the particle of interest.[36] The nanoparticles, when viewed on the STEM, are observed to be monodisperse and comprise a range of shapes and sizes. EEL spectra are recorded for every pixel in the region of interest, which encompasses the entire nanorod. From this large data set, we extract either EEL spectra at a particular spatial point (Figure 2), or we plot the loss intensity for a specific energy loss (Figure 3). The energy resolution of the EELS is determined from the full-width half-maximum of the zero-loss peak, and is 0.4–0.5 eV for the current experiments.

Conflict of Interest: The authors declare no competing financial interest.

REFERENCES AND NOTES

1. Pines, D.; Bohm, D. A Collective Description of Electron Interactions: II. Collective *vs* Individual Particle Aspects of the Interactions. *Phys. Rev.* **1952**, *85*, 338–353.
2. Ritchie, R. H. Plasma Losses by Fast Electrons in Thin Films. *Phys. Rev. B* **1957**, *106*, 874–881.
3. Raether, H., Ed. *Excitation of Plasmons and Interband Transitions by Electrons*; Springer-Verlag: Berlin, 1980.
4. Ritchie, R. H.; Howie, A. Electron-Excitation and Optical-Potential in Electron-Microscopy. *Philos. Mag.* **1977**, *36*, 463.
5. García de Abajo, F. J. Optical Excitations in Electron Microscopy. *Rev. Mod. Phys.* **2010**, *82*, 209.
6. Nelayah, J.; Kociak, M.; Stéphan, O.; García de Abajo, F. J.; Tencé, M.; Henrard, L.; Taverna, D.; Pastoriza-Santos, I.; Liz-Marzán, L. M.; Colliex, C. Mapping Surface Plasmons on a Single Metallic Nanoparticle. *Nat. Phys.* **2007**, *3*, 348.
7. Nelayah, J.; Kociak, M.; Stéphan, O.; Geuquet, N.; Henrard, L.; García de Abajo, F. J.; Pastoriza-Santos, I.; Liz-Marzán, L. M.; Colliex, C. Two-Dimensional Quasistatic Stationary Short Range Surface Plasmons in Flat Nanoprisms. *Nano Lett.* **2010**, *10*, 902–907.
8. Duan, H.; Fernández-Domínguez, A. I.; Bosman, M.; Maier, S. A.; Yang, J. K. W. Nanoplasmonics: Classical down to the Nanometer Scale. *Nano Lett.* **2012**, *12*, 1683–1689.
9. Scholl, J. A.; Koh, A.; Dionne, J. A. Quantum Plasmon Resonances of Individual Metallic Nanoparticles. *Nature* **2012**, *483*, 421.
10. Koh, A. L.; Bao, K.; Khan, I.; Smith, W. E.; Kothleitner, G.; Nordlander, P.; Maier, S. A.; McComb, D. W. Electron Energy-Loss Spectroscopy (EELS) of Surface Plasmons in Single Silver Nanoparticles and Dimers: Influence of Beam

Damage and Mapping of Dark Modes. *ACS Nano* **2009**, *3*, 3015–3022.

11. Guiton, B. S.; Iberi, V.; Li, S.; Leonard, D. N.; Parish, C. M.; Kotula, P. G.; Varela, M.; Schatz, G. C.; Pennycook, S. J.; Camden, J. P. Correlated Optical Measurements and Plasmon Mapping of Silver Nanorods. *Nano Lett.* **2011**, *11*, 3482–3488.

12. Nicoletti, O.; Wubs, M.; Mortensen, N. A.; Sigle, W.; van Aken, P. A.; Midgley, P. A. Surface Plasmon Modes of a Single Silver Nanorod: An Electron Energy Loss Study. *Opt. Express* **2011**, *19*, 15371–15379.

13. Chu, M.-W.; Myroshnychenko, V.; Chen, C. H.; Deng, J.-P.; Mou, C.-Y.; García de Abajo, F. J. Probing Bright and Dark Surface-Plasmon Modes in Individual and Coupled Noble Metal Nanoparticles Using an Electron Beam. *Nano Lett.* **2009**, *9*, 399–404.

14. Mazzucco, S.; Geuquet, N.; Ye, J.; Stéphan, O.; Van Roy, W.; Van Dorpe, P.; Henrard, L.; Kociak, M. Ultralocal Modification of Surface Plasmons Properties in Silver Nanocubes. *Nano Lett.* **2012**, *12*, 1288–1294.

15. Myroshnychenko, V.; Nelayah, J.; Adamo, G.; Geuquet, N.; Rodríguez-Fernández, J.; Pastoriza-Santos, I.; MacDonald, K. F.; Henrard, L.; Liz-Marzán, L. M.; Zheludev, N. I.; *et al.* Plasmon Spectroscopy and Imaging of Individual Gold Nanodecahedra: A Combined Optical Microscopy, Cathodoluminescence, and Electron Energy-Loss Spectroscopy Study. *Nano Lett.* **2012**asap.

16. Yurtsever, A.; Zewail, A. H. Direct Visualization of Near-Fields in Nanoplasmonics and Nanophotonics. *Nano Lett.* **2012**, *12*, 3334–3338.

17. Yurtsever, A.; van der Veen, R. M.; Zewail, A. H. Subparticle Ultrafast Spectrum Imaging in 4D Electron Microscopy. *Science* **2012**, *335*, 59–64.

18. Purcell, E. M.; Pennypacker, C. R. Scattering and Absorption of Light by Nonspherical Dielectric Grains. *Astrophys. J.* **1973**, *186*, 705.

19. Draine, B. T.; Flatau, P. J. Discrete-Dipole Approximation for Scattering Calculations. *J. Opt. Soc. Am. A* **1994**, *11*, 1491.

20. Mirsaleh-Kohan, N.; Iberi, V.; Simmons, P. D., Jr.; Bigelow, N. W.; Vaschillo, A.; Rowland, M. M.; Best, M. D.; Pennycook, S. J.; Masiello, D. J.; Guiton, B. S.; Camden, J. P. Single-Molecule Surface-Enhanced Raman Scattering: Can STEM/EELS Image Electromagnetic Hot Spots? *J. Phys. Chem. Lett.* **2012**, *3*, 2303.

21. Jackson, J. D. *Classical Electrodynamics*, 3rd ed.; J. Wiley & Sons: New York, 1999.

22. Nellist, P. D.; Pennycook, S. J. Subangstrom Resolution by Underfocused Incoherent Transmission Electron Microscopy. *Phys. Rev. Lett.* **1998**, *81*, 4156.

23. Prodan, E.; Radloff, C.; Halas, N. J.; Nordlander, P. A Hybridization Model for the Plasmon Response of Complex Nanostructures. *Science* **2003**, *302*, 419.

24. Hohenester, U.; Ditlbacher, H.; Krenn, J. R. Electron-Energy-Loss Spectra of Plasmonic Nanoparticles. *Phys. Rev. Lett.* **2009**, *103*, 106801.

25. Geuquet, N.; Henrard, L. EELS and Optical Response of a Noble Metal Nanoparticle in the Frame of a Discrete Dipole Approximation. *Ultramicroscopy* **2010**, *110*, 1075–1080.

26. García de Abajo, F. J.; Howie, A. Retarded Field Calculation of Electron Energy Loss in Inhomogeneous Dielectrics. *Phys. Rev. B* **2002**, *65*, 115418.

27. Matyssek, C.; Schmidt, V.; Hergert, W.; Wriedt, T. The T-Matrix Method in Electron Energy Loss and Cathodoluminescence Spectroscopy Calculations for Metallic Nanoparticles. *Ultramicroscopy* **2012**, *117*, 46–52.

28. Koh, A. L.; Fernández-Domínguez, A. I.; McComb, D. W.; Maier, S. A.; Yang, J. K. W. High-Resolution Mapping of Electron-Beam-Excited Plasmon Modes in Lithographically Defined Gold Nanostructures. *Nano Lett.* **2011**, *11*, 1323–1330.

29. Fussell, D. P.; McPhedran, R. C.; Martijn de Sterke, C. Decay Rate and Level Shift in a Circular Dielectric Waveguide. *Phys. Rev. A* **2005**, *71*, 013815.

30. Novotny, L., Hecht, B., Eds. *Principles of Nano-Optics*; Cambridge University Press: Cambridge, 2006.

31. García de Abajo, F. J.; Kociak, M. Probing the Photonic Local Density of States with Electron Energy Loss Spectroscopy. *Phys. Rev. Lett.* **2008**, *100*, 106804.

32. Kelly, K. L.; Coronado, E.; Zhao, L. L.; Schatz, G. C. The Optical Properties of Metal Nanoparticles: The Influence of Size, Shape, and Dielectric Environment. *J. Phys. Chem. B* **2003**, *107*, 668.

33. Draine, B. T.; Goodman, J. Beyond Clausius-Mossotti: Wave Propagation on a Polarizable Point Lattice and the Discrete Dipole Approximation. *Astrophys. J.* **1993**, *405*, 685.

34. Johnson, P. B.; Christy, R. W. Optical Constants of the Noble Metals. *Phys. Rev. B* **1972**, *6*, 4370.

35. Lynch, D. W.; Hunter, W. R. In *Handbook of Optical Constants of Solids*; Palik, E. D., Ed.; Academic Press: New York, 1985.

36. Wang, Y.; Eswaramoorthy, S. K.; Sherry, L. J.; Dieringer, J. A.; Camden, J. P.; Schatz, G. C.; Van Duyne, R. P.; Marks, L. D. A Method to Correlate Optical Properties and Structures of Metallic Nanoparticles. *Ultramicroscopy* **2009**, *109*, 1110.

37. Masiello Group, Theory of Molecular Plasmonics & Optics on the Nanoscale. http://faculty.washington.edu/masiello/Masiello_Group_Website/Home.html, 2012.